

PAPER

## Toward controlling wetting hysteresis with nanostructured surfaces derived from block copolymer self-assembly

To cite this article: Aktaruzzaman Al Hossain *et al* 2022 *Nanotechnology* **33** 455302

View the [article online](#) for updates and enhancements.

### You may also like

- [Fabrication of high-aspect-ratio aluminum oxyhydroxide nanopillars for anti-reflection surfaces](#)  
Eui Don Han, Byeong Hee Kim and Young Ho Seo
- [Effect of nanostructures on anchoring stem cell-derived neural tissue to artificial surfaces](#)  
Z Bérces, J Pomothy, Á Cs Horváth *et al.*
- [Structure-related antibacterial activity of a titanium nanostructured surface fabricated by glancing angle sputter deposition](#)  
Christina Sengstock, Michael Lopian, Yahya Motemani *et al.*



**IOP | ebooks™**

Bringing together innovative digital publishing with leading authors from the global scientific community.

Start exploring the collection—download the first chapter of every title for free.

# Toward controlling wetting hysteresis with nanostructured surfaces derived from block copolymer self-assembly

Aktaruzzaman Al Hossain<sup>1</sup> , Austin Dick<sup>1</sup>, Gregory Doerk<sup>2</sup>  and Carlos E Colosqui<sup>1,3</sup>

<sup>1</sup> Department of Mechanical Engineering, Stony Brook University, Stony Brook, NY 11794, United States of America

<sup>2</sup> Center for Functional Nanomaterials, Brookhaven National Laboratory, Upton, NY 11973, United States of America

<sup>3</sup> Department of Applied Mathematics & Statistics, Stony Brook University, Stony Brook, NY 11794, United States of America

E-mail: [carlos.colosqui@stonybrook.edu](mailto:carlos.colosqui@stonybrook.edu)

Received 11 February 2022, revised 2 June 2022

Accepted for publication 27 June 2022

Published 23 August 2022



CrossMark

## Abstract

The synthesis of nanostructured surfaces via block copolymer (BCP) self-assembly enables a precise control of the surface feature shape within a range of dimensions of the order of tens of nanometers. This work studies how to exploit this ability to control the wetting hysteresis and liquid adhesion forces as the substrate undergoes chemical aging and changes in its intrinsic wettability. Via BCP self-assembly we fabricate nanostructured surfaces on silicon substrates with a hexagonal array of regular conical pillars having a fixed period (52 nm) and two different heights (60 and 200 nm), which results in substantially different lateral and top surface areas of the nanostructure. The wetting hysteresis of the fabricated surfaces is characterized using force-displacement measurements under quasistatic conditions and over sufficiently long periods of time for which the substrate chemistry and surface energy, characterized by the Young contact angle, varies significantly. The experimental results and theoretical analysis indicate that controlling the lateral and top area of the nanostructure not only controls the degree of wetting hysteresis but can also make the advancing and receding contact angles less susceptible to chemical aging. These results can help rationalize the design of nanostructured surfaces for different applications such as self-cleaning, enhanced heat transfer, and drag reduction in micro/nanofluidic devices.

Keywords: nanostructured surfaces, wetting, block-copolymer self-assembly

(Some figures may appear in colour only in the online journal)

## 1. Introduction

Nanostructured surfaces with physical features comparable to ten to hundred molecular diameters can produce novel thermal, electrical, optical, and catalytic properties that are highly desirable for a wide range of new technological applications [1–5]. In particular, extensive studies have been conducted to understand and control the wetting behavior of micro/nanostructured surfaces because of the major implications for engineering applications such as membrane-based separation

processes, drag reduction, self-cleaning and antifouling, or pool-boiling heat transfer, among many others [6–9]. The proper combination of substrate chemistry and nanoscale physical structure can render surfaces with so-called superhydrophilic behavior [10–12], characterized by small (apparent) contact angles ( $\lesssim 10^\circ$ ), or superhydrophobic behavior with very large contact angles ( $\gtrsim 150^\circ$ ) that can be observed under static equilibrium conditions [13–15]. Moreover, the range of adhesion forces, and ‘sticky’ or ‘slippery’ behavior, that liquid water droplets, films, or meniscii

experience on superhydrophilic or superhydrophobic nanostructured surfaces is largely determined by the hysteretic behavior of the so-called advancing or receding contact angles that are observed when the three-phase contact line experiences pinning at physical defects and/or chemical heterogeneities [16–22].

Changes in the surface material chemistry due to aging and contamination and/or mechanical instabilities can lead to an irreversible loss of the desirable wetting properties and major changes in the observed contact angles and their hysteresis. For the case of superhydrophobic nanostructured surfaces it is well-established that the entrapment and collapse of a vapor film within the nanostructure, and the associated Cassie to Wenzel wetting state transition, is the main mechanism by which the same nanostructure geometry can produce widely different static contact angles [23–28]. On the other hand, the mechanisms determining the contact angle and hysteresis for (super)hydrophilic surfaces can be diverse and include hemiwicking and partial liquid infiltration, and condensation/evaporation of water within the nanostructure, as well as shear-driven failure and pinning of the contact line at nanoscale defects and heterogeneities [22, 29–34]. It is also well documented that while superhydrophobic surfaces tend to more easily preserve their wetting properties, (super) hydrophilic nanostructured surfaces are susceptible to chemical aging of the substrate, surface contamination, and changes in the ambient conditions [35–39].

In this work we study the static wetting hysteresis of nanostructured (super)hydrophilic surfaces and the feasibility to control through the nanostructure geometry its magnitude and variation when the intrinsic wettability of the silicon substrate varies over time. We employ block copolymer (BCP) self-assembly to fabricate nanostructured silicon surfaces with conical pillars having a fixed and regular period ( $\sim 52$  nm) and different heights ( $\leq 200$  nm) in order to characterize the effect of the nanostructure shape and dimensions on the static contact angle and its hysteretic behavior. Force-displacement measurements are performed with a force tensiometer to characterize the advancing and receding contact angles of the fabricated nanostructured surfaces and the non-patterned silicon substrates for short and long periods of exposure to the ambient after a surface cleaning protocol is employed. Our experimental observations are accounted for by extending the conventional models (e.g. the Wenzel [40] and Cassie–Baxter [41] equations) for equilibrium wetting in order to consider multiple metastable configurations for which the nanostructure is partially infused by water and that coexist for certain values of the Young contact angle [29–31]. Our analytical and experimental results show how the ability to tune the lateral and top area of the nanostructure can be used to control the advancing and receding contact angles, and the degree of contact angle hysteresis and their sensitivity to variations of the surface chemistry and ambient conditions. The fabrication method, analysis, and results reported in this work can be particularly helpful for the design of nanostructured surfaces with a robust wetting behavior.

## 2. Experimental

### 2.1. Nanostructured surfaces fabrication

The self-assembly of BCPs has opened new exciting directions for the design and fabrication of nanostructured materials and surfaces with regular geometric features with dimensions on the order of one to tens of nanometers [42–47]. The use of templates derived from BCP self-assembly for nanoscale patterning of substrates was first demonstrated in the late 1990s [48–50]. The surfaces studied in this work are fabricated on silicon wafers following a protocol based on BCP self-assembly as illustrated in figure 1. A silicon wafer (type N, dopant P, orientation  $\langle 100 \rangle$  from University Wafer Inc.) is first cleaned using  $O_2$  plasma at 20 W RF power, and 100 mTorr pressure for 60 s (March CS 1701). Patterning of the substrate starts with spin casting a thin layer of PS-*r*-PMMA-OH random copolymer brush, 1 wt% in propylene glycol monomethyl ether acetate (PGMEA) at 1500 rpm for 30 s (figure 1(a)). Later, thermal annealing is performed in a  $N_2$  filled hot plate at 250 °C for 5 min to graft the polymer chain and PGMEA solution is spin cast at 3000 rpm for 30 s to remove any ungrafted polymer. Cylindrical phase PS-*b*-PMMA (PS:PMMA = 64:35) with a molecular weight of  $99 \text{ kg mol}^{-1}$  is mixed to toluene by 1 wt% and spin cast at 2000 rpm for 30 s. Self assembly of the BCP in a hexagonally packed lattice (PMMA domains in a PS matrix) is obtained after performing thermal annealing at 250 °C for 20 min in a  $N_2$  enriched hot plate (figure 1(a)).

An atomic layer deposition chamber (Cambridge Nanotech Savannah S100) is used to convert selectively the PMMA domains into  $Al_2O_3$  using sequential infiltration synthesis. The sample is exposed to trimethylaluminum (TMA) and water vapor for 100 s sequentially for four times with a base pressure of  $< 1$  Torr at a constant chamber temperature of 85 °C (figure 1(b)). Intermediate  $N_2$  (100 sccm) purging steps are performed in-between the exposure steps for 100 s. After completing four cycles, a brief  $O_2$  plasma cleaning procedure (20 W, 100 mTorr, 240 s) is done to remove organic materials, which leaves a template of hexagonally packed  $Al_2O_3$  pillars to be used as the etch mask (figure 1(b)).

Using the fabricated  $Al_2O_3$  mask, silicon nanostructures are obtained (figure 1(c)) using inductively coupled plasma (ICP) etching (Oxford Plasmalab 100 ICP). The etching process starts with a ‘breakthrough’ step where  $BCl_3$  and  $Cl_2$  are mixed at 20:5 (sccm) ratio with 100 W RF power, 800 W ICP power and 10 mTorr pressure for 20 s to initiate a uniform silicon etching. Silicon nanostructures with tapered conical features are etched (figure 1(c)) by employing HBr,  $Cl_2$  and  $O_2$  gas mixture (50:50:10;sccm) at 10 mTorr pressure, 100 W RF power and 250 W ICP power for 27 and 120 s to obtain conical pillars of height 60 and 200 nm, respectively. For the 200 nm nanostructures, an additional breakthrough step is performed for 4 s with the  $BCl_3$  and  $Cl_2$  gas mixture (same recipe as the initial ‘breakthrough’ step) to remove any redeposited metal oxides on the silicon substrate. An additional etching step for 12 s is performed to obtain the desired

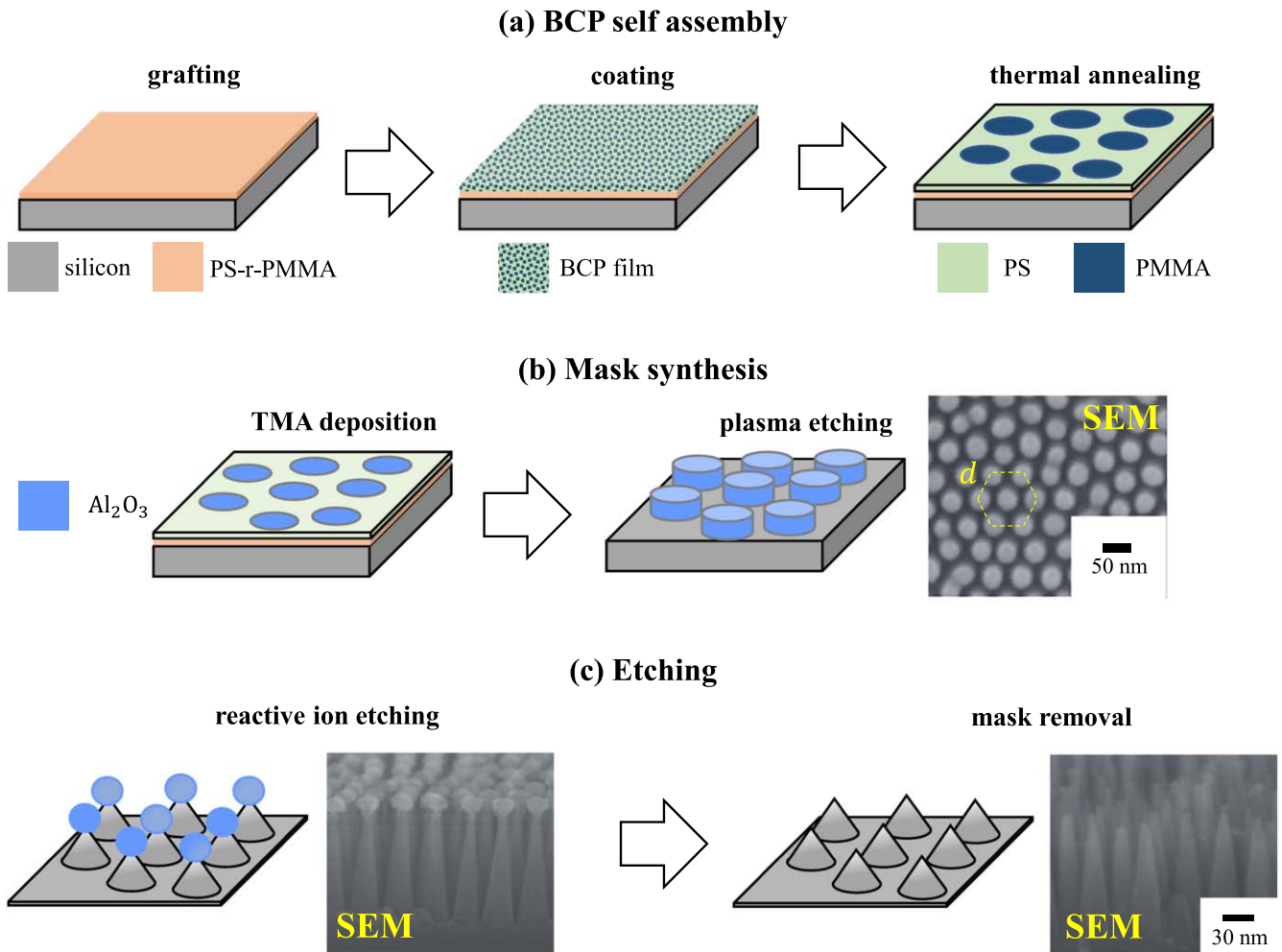


**Figure 1.** Fabrication protocol based on block copolymer (BCP) self assembly. (a) BCP self assembly procedure. (b) Mask fabrication via selective trimethylaluminum (TMA) deposition. (c) Etching steps for the nanostructure synthesis. Details for each step of the fabrication protocol are described in the main text.

conical shape with a height of 200 nm. The samples are dipped in a solution of buffered hydrofluoric acid (HF) (10:1) for 60 s to remove alumina mask deposits. To complete the process, the samples were immersed in a deionized water (DI) bath to remove any traces of HF acid, after which  $N_2$  is blown to dry the samples (figure 1(c)).

Two different nanostructured surfaces produced on a silicon wafer using the described fabrication method and using etching times of 27 s (60 nm) and 132 s (200 nm) are shown in figure 2. An additional etch step of 12 s was used for the 200 nm nanocones to remove material that redeposits during the main etch step.

Scanning electron microscopy (SEM) (see figures 2(b)–(c)) reports regular conical nanopillars with heights  $h \simeq 60$  and 200 nm that are arranged in a nearly hexagonal lattice with spacing  $d = 52 \pm 4$  nm. The reported topographic parameters for the nanostructured surfaces are obtained by using the measurement tools of the image analysis software of the SEM instrument (Hitachi S-4800); the scale bars in figure 2 are included for visual reference. The samples are tilted by 70 deg and therefore the vertical distance in the SEM images (figures 2(b)–(c)) must be corrected by a proper factor

$(1/\sin 70^\circ \simeq 1.064)$  to determine the physical height of the nanostructures; lateral distances do not require correction. The vertical distance in the SEM images is measured from the top to base area centers of the conical features as illustrated in figures 2(b)–(c). The estimates for the nanostructure dimensions reported in figure 2 correspond to rounded values for the arithmetic mean and uncertainty with a 90% confidence interval, which are obtained from a sample of 15 measurements from different SEM images of randomly selected areas for each surface sample.

As reported in figures 2(b)–(c), the average tip radius of the fabricated nanocones is  $r_t = 8$  and 7 nm and the base radius is  $r_b = 16$  and 20 nm (figure 2) for the 60 nm and 200 nm height nanostructure, respectively. The average area of a hexagonal structure cell is  $A_c = (3\sqrt{3}/2)d^2$  and thus the surface area of the tip of the cones gives the top area fraction  $\varphi_S = (2\pi/\sqrt{3})(r_t/d)^2 \simeq 0.086$  and 0.066 for the 60 nm and 200 nm structures, respectively. The lateral cone area per cell  $S_L = 3\pi(r_b + r_t)\sqrt{(r_b - r_t)^2 + h^2}$  and flat bottom area per cell  $S_B = A_c - 3\pi r_b^2$  that is not occupied by the cones, define the inner structure area fraction  $\Lambda = (S_L + S_B)/A_c = 2.49$  and 7.72 for the 60 nm and 200 nm structures (see figures 2(b)–(c))

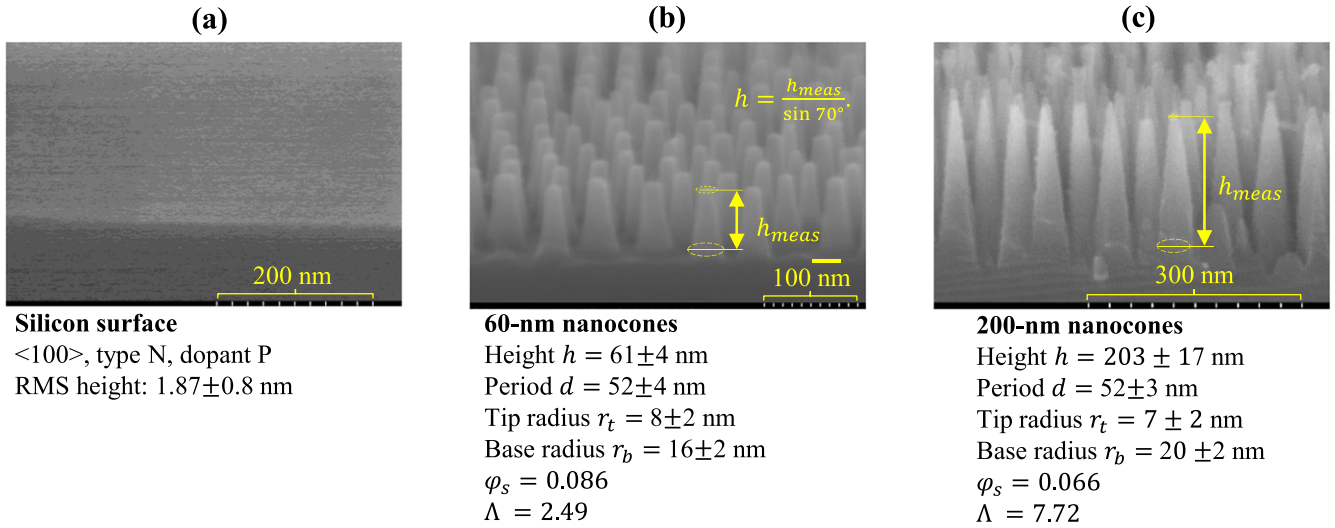


**Figure 2.** Fabricated nanostructured surfaces and geometric properties. Scanning electron microscope (SEM) images and topographic data are reported for: (a) silicon wafer, (b) 60 nm nanocones, and (c) 200 nm nanocones. Reported geometric parameters correspond to average values for the conical pillar height  $h$ , period  $d$ , tip radius  $r_t$ , and base radius  $r_b$ . These parameters are employed to estimate the top area fraction  $\varphi_s$  and lateral plus bottom area fraction  $\Lambda$  for the fabricated nanostructures.

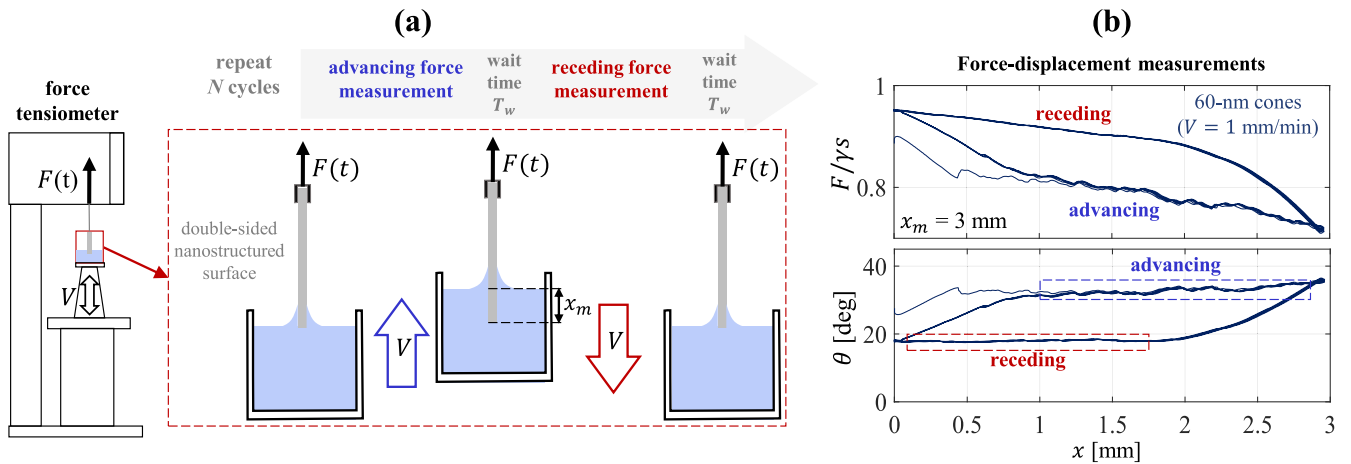


**Figure 3.** Setup. (a) Schematic of force–displacement measurements at a prescribed displacement speed  $V$  with a wait time ( $T_w \geq 0$ ) in between immersion and withdrawal stages of each measurement cycle. (b) Measured force  $F$  and contact angle  $\theta$  versus displacement  $x$  ( $\gamma$  is the water–air surface tension and  $s$  is the contact line perimeter). The reported force–displacement curve corresponds to case of the 60 nm nanostructure at speed  $V = 1 \text{ mm min}^{-1}$  and relative humidity  $\text{RH} \approx 16\%$ .

These geometric parameters reported in figure 2 are employed in the analytical wetting model to predict the equilibrium contact angle when assuming that water infiltrates the nanostructure.

## 2.2. Wetting characterization

Employing the nanostructured surfaces described in section 2.1 as Wilhelmy plates we performed force–displacement measurements in DI water with a commercial force tensiometer (Biolin Scientific, Sigma 700). The basic experimental method is illustrated in figure 3(a), the plate immersion depth is  $x_m = 3 \text{ mm}$  and the speeds employed range from  $V = 1$  to  $20 \text{ mm min}^{-1}$ , which correspond to capillary numbers  $Ca < 5 \times 10^{-6}$ . The force–displacement curve  $F(x)$  (figure 3(b)) is recorded during 10 immersion–withdrawal

cycles, staying still over a time  $T_w \geq 0$  in between the immersion and withdrawal stage. The advancing and receding contact angles (figure 3(b)) are obtained from the forces measured during the surface immersion and withdrawal after removing the buoyancy force [51, 52]. A sufficiently long wait time  $T_w \gtrsim 120 \text{ s}$  ensures that the nanostructured surface reaches equilibrium with either the ambient air and water bath, and the hemiwicking process and partial infiltration of the nanostructure reaches a stationary condition before the force  $F(x)$  is measured. The surface tension of the DI water was measured with the force tensiometer using the conventional du Nouy ring method [53, 54] and the liquid bath was replenish when its value was found below 5% from the nominal value  $\gamma, 72.3 \text{ mN m}^{-1}$ .

A single surface cleaning protocol was employed to reproduce and characterize the wetting hysteresis and the

Young contact angle variation when the silicon substrate ages, develops an oxide film, and is exposed to ambient contamination over time. First, the samples were cleaned in piranha solution ( $\text{H}_2\text{SO}_4:\text{H}_2\text{O}_2=3:1$ , volume basis) for 10 mins, rinse with DI water, and dried by blowing  $\text{N}_2$ . Plane silicon surfaces and the fabricated 60 nm and 200 nm were cleaned with this same protocol before the first set of measurements is performed. During all the reported measurements the room temperature was  $T = 23\text{ }^\circ\text{C}$ – $25\text{ }^\circ\text{C}$  and the relative humidity varied from 16% to 50%. Within the first 48–120 h after cleaning, plane silicon surfaces exhibited small hysteresis and a contact angle value  $\theta = 48 \pm 3^\circ$ . Beyond the first 120 h of measurements and depending on the ambient conditions, the plane silicon surfaces attained a substantially larger contact angles  $\theta = 72 \pm 5^\circ$ . The measured Young contact angles are in close agreement with those previously reported in the literature for piranha-cleaned silicon wafers, which showed to saturate to about  $70^\circ$  after long exposure (>100 h) to dry ambient conditions [55]. We thus adopt the measured values  $\theta_Y = 48^\circ$  for the piranha-cleaned silicon surface and  $\theta_Y = 72^\circ$  for the fully aged silicon surfaces.

### 3. Results and discussion

#### 3.1. Wetting model for nanostructured surfaces

For the case of a perfectly plane and chemically homogeneous surface the equilibrium contact angle under thermodynamic equilibrium conditions is given by the Young contact angle  $\theta_Y$ , which is prescribed by the surface energy and thus the chemical properties of the substrate. The Young contact angle is usually considered as a material property and corresponds to the single minimum of the system free energy that would be observed for an ideal plane surface under a certain ambient condition. Solid surfaces, however, present microscopic level roughness and chemical heterogeneity that give rise to the static wetting hysteresis phenomenon and the observation of a finite range of equilibrium contact angles that is bounded by the so-called static receding contact angle (lower bound) and advancing contact angle (upper bound).

Assuming a chemically homogeneous surface with regular physical structure, one can predict analytically a range of equilibrium contact angles corresponding to stable and metastable states (i.e. global and local minima of the free energy) when a liquid wets the surface and forms different interfacial configurations as illustrated in figure 4(a). The energy barriers between different stable/metastable wetting states produce the pinning of the contact line and the observation of different advancing and receding static contact angles. We will consider the general situation that the ambient phase (e.g. air and/or vapor) can be present in the nanostructure void volume in a fraction  $0 \leq \phi_b \leq 1$  under the liquid bulk, and a fraction  $0 \leq \phi_f \leq 1$  in the liquid film preceding or trailing the advancing or receding contact line (figure 4(a)). For these general conditions, minimization of the surface free

energy predicts that the equilibrium contact angle is given by

$$\cos \theta = \cos \theta_Y [\varphi_S + \Lambda(\phi_f - \phi_b)] + (1 - \varphi_S)(1 - \phi_f - \phi_b). \quad (1)$$

The expression in equation (1) is generally valid and recovers the well-known Wenzel equation [40, 56]  $\cos \theta_W = \cos \theta_Y(\varphi_S + \Lambda)$  for the ideal case that  $\phi_b = 0$  and  $\phi_f = 1$ ; i.e. for full nanostructure infiltration under the liquid bulk and a perfectly dry nanostructure on the ambient phase side (figure 4(a)). For a perfectly full and homogeneous infiltration of the nanostructure ( $\phi_b = \phi_f = 0$ ), equation (1) gives the equilibrium equation  $\cos \theta_F = \cos \theta_Y \varphi_S + 1 - \varphi_S$  that was first studied by Bico *et al* for the case of a Young contact angle and geometry combination that satisfies the critical hemiwicking condition  $\cos \theta_F < \cos \theta_W$  [57]. To characterize cases with partial and heterogeneous infiltration of the nanostructure (see figure 4(a)), we will employ equation (1) to study two characteristic conditions that give the largest advancing and receding contact angles: (I) ambient air is trapped equally under the liquid bulk and ambient phase ( $\phi_b = \phi_f > 0$ ), which gives

$$\cos \theta_I = \cos \theta_Y \varphi_S + (1 - \varphi_S)(1 - 2\phi_f); \quad (2)$$

and (II) ambient air is trapped in the preceding/receding film under the ambient phase ( $\phi_f > 0$ ) and the nanostructure is fully infiltrated by water under the liquid bulk ( $\phi_b = 0$ ), which gives

$$\cos \theta_{II} = \cos \theta_Y [\varphi_S + \Lambda\phi_f] + (1 - \varphi_S)(1 - \phi_f). \quad (3)$$

It is worth noting that in all the cases covered by equations (1)–(3) the top area of the nanostructure remains completely dry.

We can employ equation (1) to estimate the range of values that the advancing and receding contact angles can adopt for a known nanostructure geometry when the contact line moves at sufficiently low speeds  $V$  so that the capillary number  $Ca = \mu V / \gamma \ll 1$  is extremely small (here,  $\mu$  is the dynamic viscosity of water and  $\gamma$  is the water–air surface tension). For an arbitrary finite value  $\phi_f > 0$ , the contact angles  $\theta_I$  and  $\theta_{II}$  give the upper and lower bounds of equation (1), respectively; which thus corresponds to the configurations with the largest possible advancing contact angle and the lowest receding contact angle for a given partial infiltration condition. Hence, for the purpose of estimating the hysteresis range we will consider that for a known value of the Young contact angle  $\theta_Y$  and trapped air fraction  $\phi_f$ , the advancing and receding contact angles are found as  $\theta_A = \max\{\theta_W, \theta_I\}$  and lower bound  $\theta_R = \min\{\theta_F, \theta_{II}\}$ . We report in figure 4(b), the wetting hysteresis range thus computed via equation (1) for a hexagonal array ( $d = 52\text{ nm}$ ) of cylinders, truncated cones, and sharp cones, with heights  $h \leq 200\text{ nm}$ , assuming that the trapped air fraction is  $\phi = 5\%$  and for two characteristic values of the Young contact angle,  $\theta_Y \simeq 48^\circ$  and  $72^\circ$ , that were experimentally determined, respectively, for a piranha-cleaned silicon wafer with short-term exposure to the ambient and for one that has been

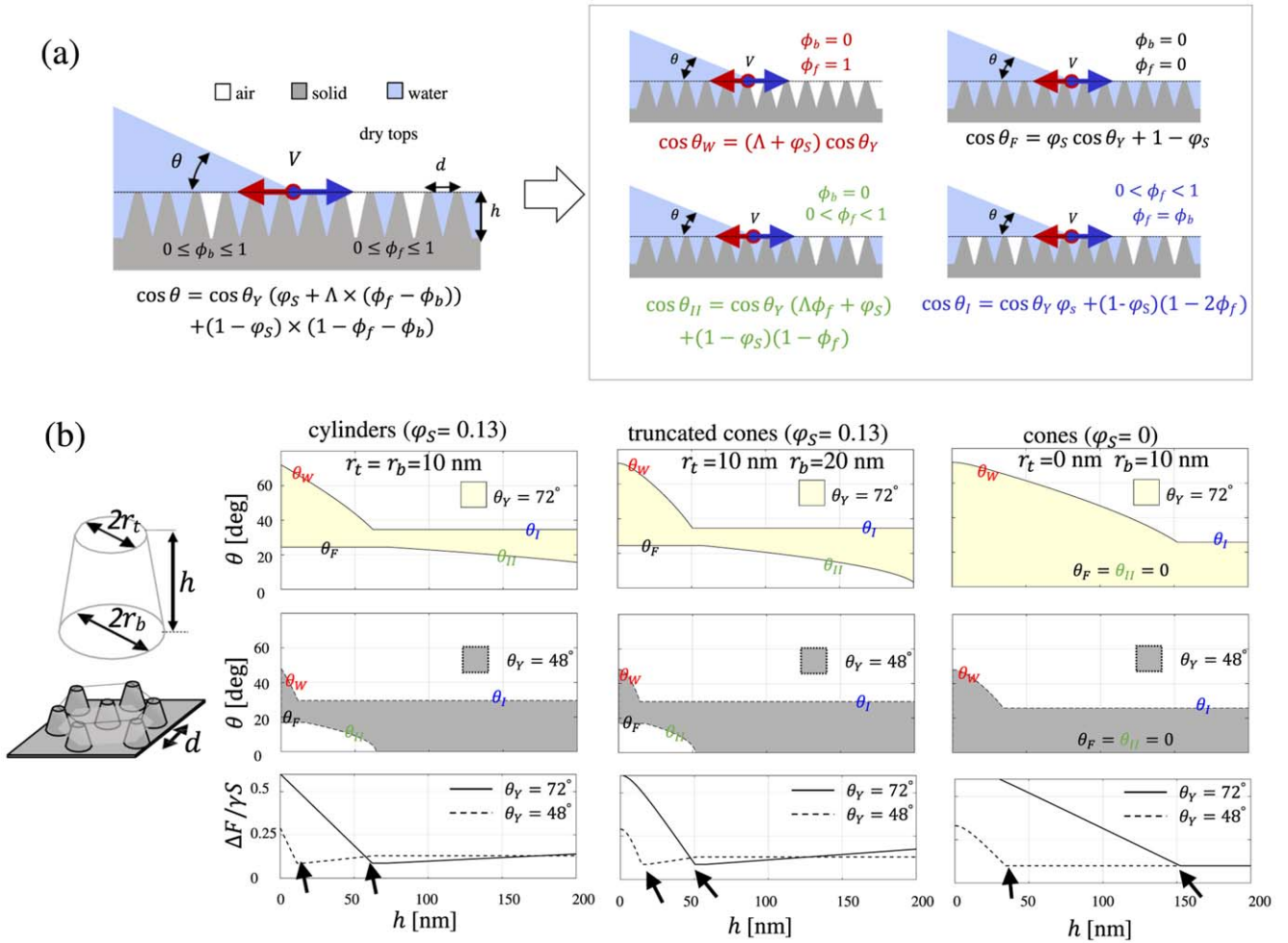


**Figure 4.** Analytical wetting model and wetting hysteresis. (a) Wetting configurations and static contact angle for full or partial infiltration of liquid in the nanostructure. Four particular configurations are considered to account for the advancing and receding contact angle. (b) Model predictions for the wetting hysteresis and adhesion force  $\Delta F$  on nanostructured surfaces with hexagonal arrays of cylinders, truncated cones, and cones of different height ( $\gamma$  is the water–air surface tension and  $s$  is the contact line perimeter). The shaded regions correspond to two different Young contact angles that were determined for piranha-clean silicon ( $\theta_Y \simeq 48^\circ$ ) and the aged silicon substrates ( $\theta_Y \simeq 72^\circ$ ). The black arrows indicate the transition to hemiwicking and water infiltration in the nanostructure.

exposed to the ambient for over 120 h. Notably, these analytical estimates show that the maximum adhesion force  $\Delta F = \gamma s (\cos \theta_R - \cos \theta_A)$ , where  $s$  is the contact line perimeter, becomes nearly insensitive to the chemical aging of the substrate, after long term exposure to the ambient, for the case of cylinders or truncated cones of sufficiently large height  $h \gtrsim 50$  nm (see figure 4(b)). The height for which the adhesion forces for different Young contact angles (figure 4(b)) become similar correspond roughly to the critical height for which  $\theta_W = \theta_F$  and spontaneous hemiwicking of the nanostructure is energetically favored [57], which results in the presence of a preceding/trailing water film. The analytical estimates in figure 4(b) can be readily computed for different values of the trapped air fraction that are feasible for certain temperature and relative humidity conditions in the ambient phase. The wetting hysteresis estimates based on equation (1) can be thus instrumental to design the nanostructure geometry for a targeted application or functionality, or rationalize

experimental observations under varying conditions of the ambient phase and surface chemistry.

### 3.2. Wetting hysteresis

This section reports and discusses the advancing and receding contact angles determined with the experimental method and surface cleaning protocol described in section 2.2. We separately analyze measurements performed within the first 48–120 h after applying the surface cleaning protocol, for which we determined that  $\theta_Y \simeq 48^\circ$ , from those measurements performed over 200 h after cleaning, for which we determined  $\theta_Y \simeq 72^\circ$  for the fully aged silicon substrate. We begin by analyzing the effect of the wait time  $T_w$  between the immersion and withdrawal stage (see figure 3), which enable us to establish whether stationary conditions are attained within the wetted nanostructure before the advancing and receding contact angle is measured. As reported in figure 5, only the

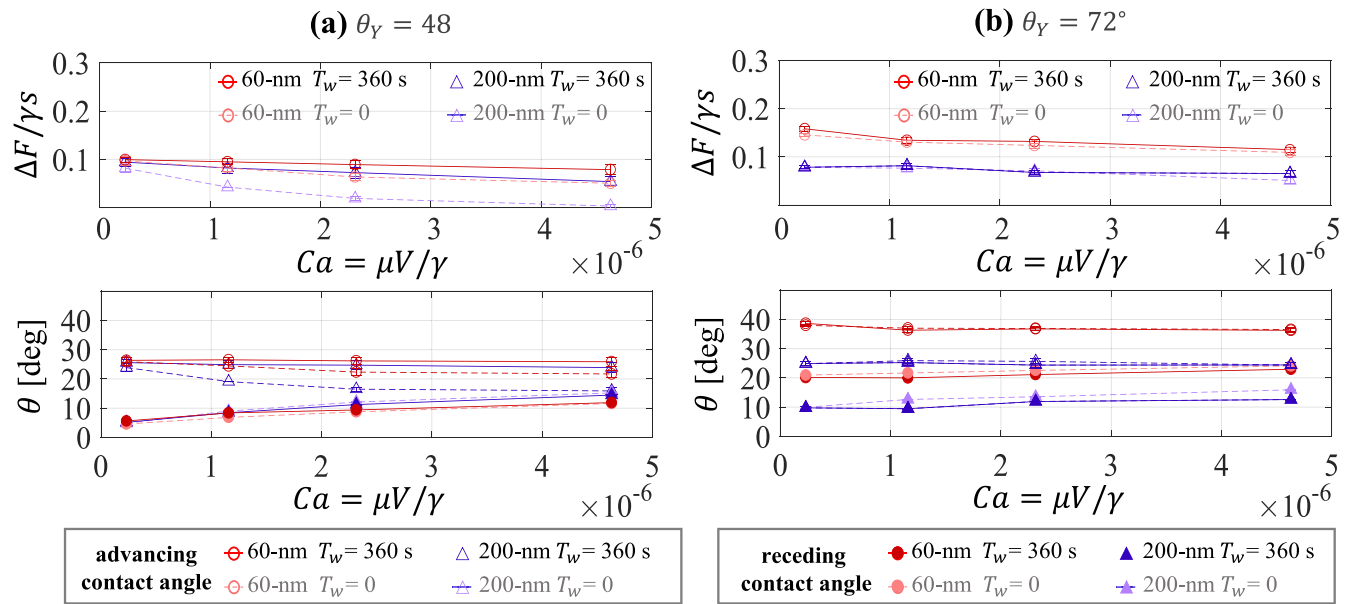


**Figure 5.** Adhesion force  $\Delta F$  (upper panel) and advancing/receding contact angles  $\theta$  (lower panels) for: (a) piranha-cleaned silicon surfaces with cleaning protocol applied within 48 h of the experimental measurement and (b) aged silicon surfaces exposed to ambient conditions for over 120 h. The wait time employed is  $T_w = 0$  (dashed lines) and  $T_w = 360$  s (solid lines) for both the 60 nm and 200 nm nanostructured surfaces ( $T = 23 \pm 1^\circ\text{C}$ ,  $\text{RH} = 16\%$ ). Attaining stationary wetting conditions, for which  $\theta$  is independent of the displacement speed, required long wait times (up to 360 s) for piranha-cleaned silicon and large displacement speeds  $V \gtrsim 5 \text{ mm min}^{-1}$ .

piranha-cleaned 200 nm nanostructured surfaces showed significant differences when the wait time was varied from 0 to 360 s and the displacement speed was larger than  $5 \text{ mm min}^{-1}$  ( $Ca \gtrsim 10^{-6}$ ), in experiments performed with a relative humidity  $\text{RH} = 16\%$  in the ambient phase. We find that for both the 60 nm and 200 nm nanostructures with a piranha-cleaned silicon substrate (figure 5(a)), mainly the advancing contact angle was affected by the amount of time that the surface is in contact with the ambient air. The key effect reported in figure 5(a) for the 200 nm nanostructure is a gradual decrease in the advancing contact angle toward the nearly constant receding value with the resulting reduction of the wetting hysteresis, as the water film that infiltrates the nanostructure is exposed to the ambient air over decreasing periods of time. The gradual vanishing of the wetting hysteresis and adhesion force  $\Delta F$  when increasing the displacement speeds (figure 5(a)) can be attributed to the substantially larger time required for the liquid to infiltrate and drain the nanostructure and reach equilibrium with the ambient phase, for the case of taller nanostructures with a hydrophilic substrate. Remarkably, both the 60 nm and 200 nm nanostructured surfaces with lower degree of hydrophilicity after over 200 h exposure to the ambient air (figure 5(b)) do not show significant variations with the wait time between immersion and withdrawal, which seems to indicate that stationary wetting conditions are attained within a few seconds.

In what follows, we compare analytical predictions from equation (1) and experimental results for the cases that the nanostructured surfaces reached stationary wetting conditions, which are observed in all cases after sufficiently long wait times of over 240 s between the immersion and withdrawal of the samples. It is assumed that sufficient time

elapses after the nanostructured surface is put in contact with the liquid bath, a metastable wetting configuration is attained with partial infiltration of water in the nanostructure and a small trapped air fraction  $\phi_f > 0$ . The results in figures 6(a)–(b) correspond to measurements taken at similar ambient conditions with a relative humidity  $\text{RH} = 16\%$  and temperature  $T = 22^\circ\text{C}$ – $24^\circ\text{C}$ . For these ambient conditions with low air moisture, we find that analytical predictions from equations (1)–(3), which assume the top of the cones remain dry, can account closely for experimental measurements when employing small trapped air fractions  $\phi_f = 2.5\%$ – $4\%$  both for the cases of piranha-cleaned silicon surfaces and those that fully aged after over 200 h of exposure to the ambient air. The entrapped air fraction  $\phi_f$  in the analytical predictions for  $\theta_I$  and  $\theta_{II}$  (i.e. wetting states I and II) was treated as an adjustable parameter to fit the experimental results. We find that employing small but finite (2.5%–4%) trapped air fractions was necessary to rationalize the contact angles measured for the studied nanostructured surfaces and ambient conditions with low relative humidity (i.e.  $\text{RH} = 16\%$ ). This supports the assumption that the nanostructure is not perfectly and completely infused by liquid as assumed in the Wenzel and hemiwicking states that predict the angles  $\theta_W$  and  $\theta_F$ , respectively, in the limit that  $\phi_f = 0$ .

It is important to note that the 200 nm nanostructured surfaces satisfy the condition  $\theta_F > \theta_W$  for favoring hemiwicking [57] both for the piranha-cleaned silicon ( $\theta_Y = 48^\circ$ ) and aged silicon substrates ( $\theta_Y = 72^\circ$ ). As a result, the advancing/receding contact angles and wetting hysteresis for the 200 nm nanostructure surfaces can be accounted for by the equations (2)–(3) that describe the metastable wetting states I and II with a preceding/trailing water film (see figure 6(a)). Only the 60 nm nanostructure with lower

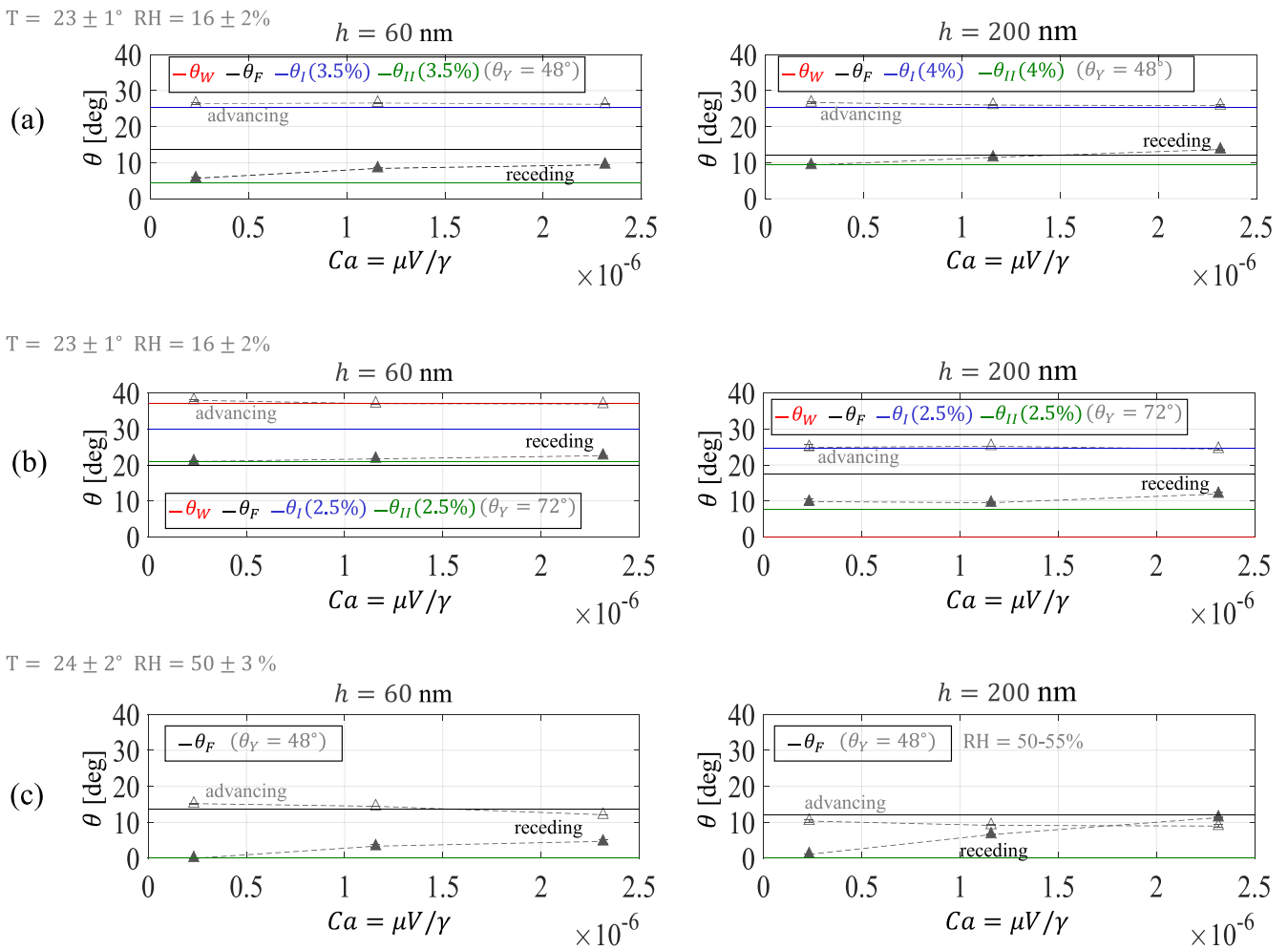


**Figure 6.** Advancing and receding contact angles for different surface chemistry and ambient conditions for the studied 60 nm and 200 nm nanostructured surfaces. (a) Piranha-cleaned silicon (up to 65 h of ambient exposure) and low air humidity ( $RH = 16 \pm 2\%$ ). (b) Aged silicon substrate (over 120 h of ambient exposure) and low air humidity ( $RH = 16 \pm 2\%$ ). (c) Piranha-cleaned silicon (less than 120 h of ambient exposure) and moderate air humidity ( $RH = 50 \pm 3\%$ ). The markers indicate experimental results for the advancing (empty triangles) and receding contact (filled triangles) angles. Analytical predictions from equations (1)–(3) (see legend) are reported for the Young contact angles  $\theta_Y = 48^\circ$  and  $\theta_Y = 72^\circ$  determined for each case, and a trapped air fraction  $\phi_f = 2.5\%$ – $4\%$  for the low moisture conditions.

hydrophilicity after long exposure to the ambient satisfy the thermodynamic conditions to observe a Wenzel wetting state, and as expected the advancing contact angle for this case is predicted by the conventional Wenzel equation (see figure 6(b)). The emergence of the Wenzel state for the 60 nm aged silicon nanostructure results in a large wetting hysteresis with  $\theta_A \simeq 40^\circ$  after long-term ambient exposure (see figure 6(b)).

Comparing the results in figures 5 and 6 corresponding to short- and long-term exposure to a low-moisture ambient, we find that the taller 200 nm nanostructure presents less variation in the value of their advancing and receding contact angles and relatively small wetting hysteresis with  $\theta_A - \theta_R \simeq 15^\circ$ . These results indicate that taller nanostructures that favor hemiwicking for higher values of the Young contact angles and the infiltration of a larger water volume can display macroscopic wetting properties that are more stable when the surface is exposed to the ambient for long periods of time.

An additional important observation is reported in figure 6(c), which correspond to measurements for piranha-cleaned silicon surfaces that are in contact with a high-moisture environment with  $RH \simeq 50\%$ . Under such conditions, both the 60 nm and 200 nm nanostructured surfaces present so-called superhydrophilic behavior with advancing and receding contact angles roughly below  $10^\circ$  and a very low contact angle hysteresis (figure 6(c)). A vanishingly small value of the receding contact angle (see figure 6(c)) cannot be accounted for via equation (1), which assumes that the top surface of the conical pillars remains fully dry. It is feasible that under a favorable combination of surface chemistry and humid ambient conditions, the receding contact line can wet, at least partially the top surface of the nanopillars where water molecules can be adsorbed [55], which thus results in nearly perfect wetting conditions that are not accounted for by equation (1). As reported in previous studies with silicon surfaces, superhydrophilic or superwetting behavior is found to not be robust and vanishes when the surface is exposed to the ambient for over 48 h (see figure 6(c)).

## 4. Conclusions

In summary, we have fabricated nanostructured surfaces on silicon with well controlled geometrical features by employing a protocol based on BCP self assembly and carefully characterized their advancing and receding contact angle over time as the silicon substrate is exposed to the ambient, ages and develops an oxide film. The silicon substrate when exposed to the ambient air for several hours or days presents substantially larger Young contact angles due to changes in the surface chemistry due to chemical aging and contamination, which significantly affects the contact angles and wetting hysteresis of the nanostructured surfaces. The substrate aging phenomenon is difficult to prevent without chemical passivation. Our experimental results show that surfaces with taller nanostructures, which favor hemiwicking and the nanostructure infiltration by water for a wider range of Young contact angles, can present more stable wetting properties and lower adhesion forces when exposed to ambient air over long periods of time.

We formulated a general analytical model for the static (advancing/receding) contact angles that correspond to metastable wetting configurations with partial infiltration of the nanostructure, that are characterized by a non-zero fraction of trapped air within the nanostructure void volume. The analytical model accounts for our experimental observations when assuming small trapped air fractions between 2.5% and 4% for ambient conditions with low relative humidity  $RH \lesssim 20\%$ . For the studied nanostructured surfaces, we have observed superhydrophilic or superwetting behavior with vanishingly small contact angles and wetting hysteresis only for cases with a piranha-cleaned silicon substrate and moderate to large relative humidity conditions. The experimental and analytical results in this work indicate that geometric properties of the nanostructure, such as the lateral and top area, can be modified to control the wetting hysteresis and mitigate the effects associated with chemical aging of the substrate material. These findings can help design nanostructured surfaces for engineering applications where the surface needs to be exposed to the ambient over long periods of time.

## Acknowledgments

This work was supported by the National Science Foundation (Award CBET-2016204). CEC acknowledges support from the Center for Mesoscale Transport Properties, an Energy Frontier Research Center supported by the DOE-BES, under Award DE-SC0012673. All nanofabrication work was performed at the Center for Functional Nanomaterials (CFN), which is a U.S. Department of Energy Office of Science User Facility, at Brookhaven National Laboratory under Contract No. DE-SC0012704.

## Data availability statement

The data that support the findings of this study are available upon reasonable request from the authors.

## ORCID iDs

Aktaruzzaman Al Hossain  <https://orcid.org/0000-0002-4051-9101>

Gregory Doerk  <https://orcid.org/0000-0002-2933-2047>

## References

- [1] Kim D E, Yu D I, Jerng D W, Kim M H and Ahn H S 2015 *Exp. Therm. Fluid Sci.* **66** 173–96
- [2] Ko H, Singamaneni S and Tsukruk V V 2008 *Small* **4** 1576–99
- [3] Khodasevych I E, Wang L, Mitchell A and Rosengarten G 2015 *Adv. Opt. Mater.* **3** 852–81
- [4] Ge M et al 2017 *Int. J. Hydrog. Energy* **42** 8418–49
- [5] Higgins S G, Becce M, Belessiotis-Richards A, Seong H, Sero J E and Stevens M M 2020 *Adv. Mater.* **32** 1903862
- [6] Krupin T N, Taylor J A, Schneider T M and Yang S 2004 *Langmuir* **20** 3824–7
- [7] Nosonovsky M and Bhushan B 2009 *Curr. Opin. Colloid Interface Sci.* **14** 270–80
- [8] Nishimoto S and Bhushan B 2013 *RSC Adv.* **3** 671–90
- [9] Shojaeian M and Koşar A 2015 *Exp. Therm. Fluid Sci.* **63** 45–73
- [10] Drelich J and Chibowski E 2010 *Langmuir* **26** 18621–3
- [11] Drelich J, Chibowski E, Meng D D and Terpilowski K 2011 *Soft Matter* **7** 9804–28
- [12] Fernández-Blázquez J P, Fell D, Bonaccorso E and Del Campo A 2011 *J. Colloid Interface Sci.* **357** 234–8
- [13] Ma M and Hill R M 2006 *Curr. Opin. Colloid Interface Sci.* **11** 193–202
- [14] Li X M, Reinhoudt D and Crego-Calama M 2007 *Chem. Soc. Rev.* **36** 1350–68
- [15] Xiu Y, Liu Y, Hess D W and Wong C 2010 *Nanotechnology* **21** 155705
- [16] McHale G, Shirtcliffe N and Newton M 2004 *Langmuir* **20** 10146–9
- [17] Li W and Amirfazli A 2005 *J. Colloid Interface Sci.* **292** 195–201
- [18] Yu D I, Kwak H J, Doh S W, Kang H C, Ahn H S, Kiyofumi M, Park H S and Kim M H 2015 *Int. J. Heat Mass Transfer* **90** 191–200
- [19] Chang F M, Hong S J, Sheng Y J and Tsao H K 2009 *Appl. Phys. Lett.* **95** 064102
- [20] Rothstein J P 2010 *Annu. Rev. Fluid Mech.* **42** 89–109
- [21] Xu W and Choi C H 2012 *Phys. Rev. Lett.* **109** 024504
- [22] Zhang S, Huang J, Chen Z, Yang S and Lai Y 2019 *J. Mater. Chem. A* **7** 38–63
- [23] Checco A, Hofmann T, DiMasi E, Black C T and Ocko B M 2010 *Nano Lett.* **10** 1354–8
- [24] Teisala H, Tuominen M, Aromaa M, Stepien M, Makela J M, Saarinen J J, Toivakka M and Kuusipalo J 2012 *Langmuir* **28** 3138–45
- [25] Papadopoulos P, Mammen L, Deng X, Vollmer D and Butt H J 2013 *Proc. Natl. Acad. Sci.* **110** 3254–8
- [26] Liu Y and Zhang X 2013 *J. Chem. Phys.* **138** 014706
- [27] Checco A, Ocko B M, Rahman A, Black C T, Tasinkevych M, Giacomello A and Dietrich S 2014 *Phys. Rev. Lett.* **112** 216101
- [28] Wang Y, Li X, Ren S, Alem H T, Yang L and Lohse D 2017 *Soft Matter* **13** 5381–8
- [29] Ishino C and Okumura K 2008 *Eur. Phys. J. E* **25** 415–24
- [30] Kavousanakis M E, Colosqui C E, Kevrekidis I G and Papathanasiou A G 2012 *Soft Matter* **8** 7928–36
- [31] Bormashenko E 2015 *Adv. Colloid Interface Sci.* **222** 92–103

- [32] Zhang P, Wang S, Wang S and Jiang L 2015 *Small* **11** 1939–46
- [33] Colosqui C E, Wexler J S, Liu Y and Stone H A 2016 *Phys. Rev. Fluids* **1** 064101
- [34] Zheng D, Choi C H, Sun G and Zhao X 2020 *ACS Appl. Mater. Interfaces* **12** 30925–31
- [35] Permpoon S, Houmard M, Riassetto D, Rapenne L, Berthomé G, Baroux B, Joud J and Langlet M 2008 *Thin Solid Films* **516** 957–66
- [36] Zhang L, Zhao N and Xu J 2014 *J. Adhes. Sci. Technol.* **28** 769–90
- [37] Otitoju T, Ahmad A and Ooi B 2017 *J. Ind. Eng. Chem.* **47** 19–40
- [38] Al Hossain A, Yang M, Checco A, Doerk G and Colosqui C E 2020 *Appl. Mater. Today* **19** 100553
- [39] Song Z, Lin E S, Zhu J, Ong J W, Abid H A, Uddin M H, Liew O W and Ng T W 2021 *Colloids Surf. A* **613** 126097
- [40] Wenzel R N 1936 *Ind. Eng. Chem.* **28** 988–94
- [41] Cassie A and Baxter S 1944 *Trans. Faraday Soc.* **40** 546–51
- [42] Bates F S and Fredrickson G H 1990 *Annu. Rev. Phys. Chem.* **41** 525–57
- [43] Segalman R A 2005 *Mater. Sci. Eng. R* **48** 191–226
- [44] Black C T, Ruiz R, Breyta G, Cheng J Y, Colburn M E, Guarini K W, Kim H C and Zhang Y 2007 *IBM J. Res. Dev.* **51** 605–33
- [45] Park C, Yoon J and Thomas E L 2003 *Polymer* **44** 6725–60
- [46] Ishchenko O M, Krishnamoorthy S, Valle N, Guillot J, Turek P, Fehete I and Lenoble D 2016 *J. Phys. Chem. C* **120** 7067–76
- [47] Suresh V, Chew A B, Tan C Y L and Tan H R 2022 *Nanotechnology* **33** 135303
- [48] Park M, Harrison C, Chaikin P M, Register R A and Adamson D H 1997 *Science* **276** 1401–4
- [49] Mansky P et al 1995 *J. Mater. Sci.* **30** 1987–92
- [50] Mansky P, Harrison C, Chaikin P, Register R and Yao N 1996 *Appl. Phys. Lett.* **68** 2586–8
- [51] Ramé E 1997 *J. Colloid Interface Sci.* **185** 245–51
- [52] Karim A M and Kavehpour H P 2018 *Colloids Surf. A* **548** 54–60
- [53] Du Noüy P L 1919 *J. Gen. Physiol.* **1** 521
- [54] Macy R 1935 *J. Chem. Educ.* **12** 573
- [55] Yang X, Zhong Z, Diallo E, Wang Z and Yue W 2014 *Mater. Sci. Semicond. Process.* **26** 25–32
- [56] Wenzel R N 1949 *J. Phys. Chem.* **53** 1466–7
- [57] Bico J, Thiele U and Quere D 2002 *Colloids Surf. A* **206** 41–6